

The low dark matter content of the lenticular galaxy NGC 3998

Nicholas Boardman^{1*}, Anne-Marie Weijmans¹, Remco van den Bosch², Ling Zhu², Akin Yildirim², Glenn van de Ven², Michele Cappellari³, Tim de Zeeuw⁴, Eric Emsellem⁴, Davor Krajnović⁶, Thorsten Naab⁷

¹*School of Physics and Astronomy, University of St Andrews, KY16 9SS UK*

²*Max Planck Institute for Astronomy, Königstuhl 17, D-69117 Heidelberg, Germany*

³*Sub-department of Astrophysics, Department of Physics, University of Oxford, Denys Wilkinson Building, Keble Road, Oxford OX1 3RH*

⁴*European Southern Observatory, Karl-Schwarzschild-Str. 2, 85748 Garching, Germany*

⁵*Sterrewacht Leiden, Leiden University, Postbus 9513, 2300 RA, Leiden, The Netherlands*

⁶*Leibniz-Institut für Astrophysik Potsdam (AIP), An der Sternwarte 16, D-14482 Potsdam, Germany*

⁷*Max-Planck-Institut für Astrophysik, Karl-Schwarzschild-Str. 1, 85741 Garching, Germany*

Accepted 2016 May 13. Received 2016 May 13; in original form 2016 February 12

ABSTRACT

We observed the lenticular galaxy NGC 3998 with the Mitchell Integral-Field Spectrograph and extracted line-of-sight velocity distributions out to 3 half-light radii. We constructed collisionless orbit models in order to constrain NGC 3998’s dark and visible structure, using kinematics from both the Mitchell and SAURON instruments. We find NGC 3998 to be almost axisymmetric, seen nearly face on with a flattened intrinsic shape - i.e., a face-on fast-rotator. We find an I-band mass-to-light ratio of $4.7^{+0.32}_{-0.45}$ in good agreement with previous spectral fitting results for this galaxy. Our best-fit orbit model shows a both a bulge and a disc component, with a non-negligible counter-rotating component also evident. We find that relatively little dark matter is needed to model this galaxy, with an inferred dark mass fraction of just $(7.1^{+8.1}_{-7.1})\%$ within one half-light radius.

Key words: dark matter - galaxies: elliptical and lenticular, CD - galaxies: ISM - galaxies: kinematics and dynamics - galaxies: structure - ISM: kinematics and dynamics

1 INTRODUCTION

Early-type galaxies (ETGs) are amongst the most highly-evolved structures in the Universe. Lying in the red sequence of galaxies, they are defined chiefly by their predominantly-old stellar populations. Imaging studies have repeatedly shown the massive ($M \geq 10^{11} M_{\odot}$) ETG population to be smaller and more compact at $z \simeq 2$ than in the present day (Trujillo et al. 2006; Cimatti et al. 2012; van Dokkum et al. 2010). Lower-mass galaxies appear to grow their mass in a far more uniform way, which suggests their growth to be dominated by in-situ star formation (van Dokkum et al. 2013).

The ATLAS^{3D} survey (Cappellari et al. 2011) rep-

resents one of the first systematic studies of ETGs using integral-field spectroscopy. The survey includes two-dimensional spectroscopy with the SAURON instrument (Bacon et al. 2001) for a volume-limited sample of 260 nearby ETGs, expanding upon the earlier SAURON survey (de Zeeuw et al. 2002). SAURON observations have revealed a wide range of ETG kinematic structures. Massive ETGs mostly show little net rotation and are termed “slow rotators” (SRs), while less-massive ETGs are largely dominated by rotation and show evidence of stellar discs (Cappellari et al. 2007; Emsellem et al. 2007, 2011; Krajnović et al. 2013); these are labelled “fast rotators” (FRs). Individual ETGs show a wide range of kinematic substructures, which include kinematic twists and kinematically-decoupled cores (Krajnović et al. 2011).

Analyses of the ATLAS^{3D} data have suggested that while FRs seem to smoothly connect to their later-type

* E-mail: nfb@st-andrews.ac.uk

counterparts (including various and complex formation histories), SRs had a faster and more violent history (Cappellari 2013) SRs appear to form in an "inside-out" way, as in the "two-phase" model of ETG formation (Oser et al. 2010): a central core forms at high redshift via dissipative processes (e.g. Hoffman et al. 2010), with late-stage growth then dominated by dry mergers and accretion (e.g. Naab et al. 2009; Oser et al. 2010, 2012; Bai et al. 2014). Compact high-redshift ETGs, meanwhile, are thought to have formed in a similar manner to nearby SRs (Barro et al. 2013; van Dokkum et al. 2015). This picture explains the strong correlations between the galaxy velocity dispersion σ and other properties of local ETGs for galaxy masses below $\simeq 2 \times 10^{11} M_{\odot}$ (Cappellari et al. 2013b): σ acts as a tracer for the bulge mass fraction, reflecting the growth of the bulge as a spiral becomes a fast-rotating ETG (see, e.g. Cappellari 2016, for a review).

Several recent results have complicated the above picture, at least in regard to FRs. The concentration and stellar angular momentum of lenticular galaxies appear incompatible with them having passively evolved from spirals, implying that mergers are needed to reduce the angular momentum (Querejeta et al. 2015). Major mergers are one possibility (Querejeta et al. 2015), but simulations of repeated minor mergers have also produced realistic galaxies (Bournaud et al. 2007). The star-formation rate of star-forming galaxies in groups shows no evidence of being globally lower than for star forming galaxies in the field (Lin et al. 2014), which implies quenching to be a rapid process; this further supports mergers as significant FR quenching mechanism.

One way to further investigate the development of FRs is to study the kinematics of their outer regions. Dry accretion episodes, are expected to produce an excess of radial orbits beyond the central half-light radius (or effective radius, R_e) (Wu et al. 2014), which is beyond SAURON's field of view (FOV) for most galaxies in the ATLAS^{3D} sample. Gas rich mergers and interactions, meanwhile, are expected to result in an excess of rotational orbits within a galaxy (Röttgers et al. 2014);

Kinematic studies of ETGs beyond $1 R_e$ have yielded mixed results to date. (Arnold et al. 2014) present stellar kinematics for 22 nearby massive ETGs out to $2 - 4 R_e$ and report a significant fraction of them to show abrupt drops in their angular momentum profiles beyond $1 R_e$; they argue that late dry accretion must have been important for these systems. (Raskutti et al. 2014) report much smoother angular momentum profiles for their ETGs out to $2 - 5 R_e$, though they note that the higher masses of their sample could be a potential confounding factor. Kinematic measurement for ETGs beyond $1 R_e$ have also been made using planetary nebular and/or globular cluster measurements (e.g. Douglas et al. 2007; Coccato et al. 2013; Pota et al. 2013), as well as using stellar measurements from long-slit spectra (e.g. Kronawitter et al. 2000; Khoperskov et al. 2014).

Schwarzschild (1979) orbit-based dynamical modelling is an ideal tool for studying a galaxy's kinematic structure in further detail. Here, a galaxy is modelled as a superposition of collisionless stellar orbits, with no prior assumptions made on the nature of these orbits. Orbit-based dynamical modelling allows various galaxy proper-

ties such as the stellar mass-to-light ratio and the galaxy viewing angle to be constrained, and it also enables the distribution of stellar orbits to be studied as a function of position.

The role of dark matter is also important to consider here. From the hierarchical cold dark matter paradigm (Blumenthal et al. 1984), all ETGs should exist within massive dark matter halos. Dynamical modelling of ATLAS^{3D} data has yielded a median dark matter fraction of 13% within $1 R_e$ (Cappellari et al. 2013a); thus, dark matter must be considered when constructing wide-field dynamical models of ETGs.

Orbit modelling has been used to investigate ETG dark halos in the past (e.g. Weijmans et al. 2009; Cappellari et al. 2013a), but such studies remain rare for complete two-dimensional stellar kinematics beyond the central effective radius. Yıldırım et al. (2015) model two compact ETGs out to $3-4 R_e$, and find dark matter to be necessary to model one (MRK 1216) but not the other (NGC 1277). Yıldırım et al. (2016) model the compact ETG NGC 1286 out to $5 R_e$ and also find models with a massive dark halo to fit the galaxy best.

The Mitchell Integral-Field Spectrograph (Hill et al. 2008), formerly VIRUS-P, is particularly well-suited to investigating ETGs' structures beyond $1 R_e$. It features a 1.68×1.68 arcminute field of view, as well as large fibres (radius $2.08''$) which reduce the need for spatial binning.

In this paper, we focus on a single ETG: the lenticular galaxy NGC 3998, which we observed with the Mitchell Spectrograph over several nights. We extracted kinematics out to three R_e up to the fourth Gauss-Hermite moment. We then used triaxial collisionless orbit models (van den Bosch et al. 2008) to constrain the dark matter content, intrinsic shape, stellar mass-to-light ratio (M/L) and orbital structure of this galaxy. This paper serves to showcase our Mitchell Spectrograph data as well as a variety of techniques we are employing; we will present similar work on a larger set of galaxies in a future publication.

The structure of this paper is as follows. We discuss our observations and data reduction in section 2. We describe the extraction of kinematic data in section 3, and we discuss the orbit-modelling method in section 4. We present the results of our modelling in section 5. We discuss our findings in section 6 and then conclude in section 7.

We assume a Hubble parameter of $h = 0.73$ throughout this work.

2 SAMPLE AND DATA REDUCTION

NGC 3998 is a bright, nearby (13.7 Mpc; Cappellari et al. 2011, and references therein) lenticular galaxy with a powerful LINER nucleus in its centre (e.g. Dressel & Galagher 2001). The galaxy's brightness, combined with its simple morphology, makes it an ideal target for dynamical modelling (e.g. Walsh et al. 2012). NGC 3998 is part of the ATLAS^{3D} sample and has been detected in H I (Serra et al. 2012). We provide a brief summary of NGC 3998 in Table 1.

We took 38 exposures of NGC 3998 with the Mitchell Spectrograph (Hill et al. 2008) in the high-resolution red

Type	S0
RA(°)(J2000)	179.484039
DEC(°)(J2000)	55.453564
Distance(Mpc)	13.7
$\log(R_e)('')$	1.30
$\log(L_I)(L_\odot)$	10.15
M_{bh}	$8.1 \times 10^8 M_\odot$

Table 1. Summary of NGC 3998’s properties. The black hole mass M_{bh} and I-band luminosity L_I are from Walsh et al. (2012). All other values are from Cappellari et al. (2011) and references therein.

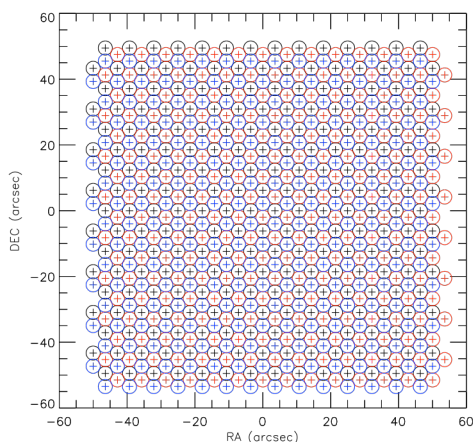


Figure 1. Mitchell Spectrograph first (black crosses), second (red crosses) and third (blue crosses) dither positions. The circles around each point represent the fibre cross sections. We achieve good sky coverage by combining all three dithers

setup (spectral range 4770Å - 5430Å), over nine nights between the 9th and 18th of March, 2010. Each exposure was taken for 1800s, producing a total time on source of 19 hours. We observed at three dither positions in order to fully sample the field of view; this is illustrated in Figure 1. Since the spectrograph lacks dedicated sky fibres, we took sky exposures of 900s each so as to bracket pairs of science observations. We took bias frames, flat frames and arc frames at the beginning and end of each night. We selected either the dawn or dusk arcs and flats for each night to minimise the temperature differences between those and the observations. We used Ne+Cd comparison lamps for all arc frames.

We carried out most of the data reduction using the VACCINE pipeline (Adams et al. 2011). VACCINE is designed to avoid resampling of data, which can result in propagated errors, and uses techniques similar to those proposed by Kelson (2003). It subtracts science frames for overscan and bias, calculates tracing and wavelength solutions for each fibre, calculates a corresponding sky frame for each science frame and collapses each fibre down into a 1D spectrum. Our reduction also included the LA-Cosmic

algorithm of van Dokkum (2001), which is designed to mask all frames of cosmic rays.

We calculated the spectral resolution of the instrument using the acquired arc frames. We fitted Gaussians to the 5154.660 and 5400.56Å emission lines across all nine nights, in order to obtain the spectral full-width at half maximum (FWHM) as a function of fibre position. We found the FWHM to vary smoothly as a function of fibre position, with values ranging from 1.26 to 1.63Å. Our maximum FWHM corresponds to an intrinsic instrumental velocity dispersion of $\sigma = 41\text{km/s}$.

We constructed sky frames from sky exposures taken before and after a given galaxy frame. We used the method and code of Blanc et al. (2013), which allows for non-linear variations of the sky spectrum in both time and wavelength space, and then sky-subtracted all science frames. We combined all reduced science frames into a single spectral datacube, in which all spectra were interpolated onto a common linear scale. We then broadened all spectra in the cube to a common FWHM of 1.63Å.

We masked three fibres located at the edges of the CCD chip during data reduction, in order to remove fibres not completely on the chip. These fibres are all located at the edges of our FOV, and so removing them does not have a big impact on our data. We also excluded two fibre positions from our analysis which we found to be contaminated by foreground objects.

3 KINEMATICS

In this section, we describe the extraction of NGC 3998’s line-of-sight stellar kinematics up to the fourth Gauss-Hermite moment (V, σ, h_3, h_4). In section 3.1, we provide an overview of our chosen method and present our results obtained from the Mitchell Spectrograph. In section 3.2, we report our re-extraction of SAURON kinematics with our chosen stellar library, for maximum consistency between the two instruments’ results.

3.1 Mitchell Kinematics

To improve the signal-to-noise (S/N) at the galaxy’s outermost regions, we binned spectra using the publicly available Voronoi Binning algorithm (Cappellari & Copin 2003). We chose a minimum S/N target of 40 per spectral resolution element to ensure that all four kinematic moments could be reliably extracted; this target was already satisfied for many of the spectra, resulting in relatively little binning.

We extracted stellar kinematics using the publicly available penalised pixel fitting (pPXF) software (Cappellari & Emsellem 2004). The pPXF routine fits an optimised template $G_{mod}(x)$ to a galaxy spectrum $G(x)$ directly in pixel space after logarithmically rebinning the spectrum in the wavelength direction, thereby recovering the LOSVD of that spectrum. The model spectra take the form

$$G_{mod}(x) = \sum_{k=1}^K w_k [\mathcal{L}(cx) * T_k](x) + \sum_{l=0}^L b_l \mathcal{P}_l(x) \quad (1)$$

where $\mathcal{L}(cx)$ is the broadening function, T_k a set of distinct stellar templates and w_k the optimal weights of those templates, with $*$ describing convolution. $\mathcal{P}_l(x)$ are Legendre polynomials of order l and are used to adjust for low-frequency differences between model and data, with b_l the corresponding weights.

The pPXF routine requires an input "bias parameter" which biases the recovered LOSVD towards a perfect gaussian when h_3 and h_4 become ill-determined, in order to prevent spurious solutions. We optimised this parameter using the simulation code included in the pPXF package, with the standard prescription that the deviation between input and output h_3 and h_4 should be less than $\text{rms}/3$ for values of σ greater than three times the velocity scale. This led to an optimal bias of 0.2 for our target S/N of 40.

For stellar templates, we used the medium-resolution (FWHM = 0.51\AA) ELODIE library (Prugniel & Soubiran 2001) of observed stars. We selected stars from the ELODIE library by performing a set of initial pPXF fits on elliptical annuli, which were constructed using ATLAS^{3D} ellipticity data (Krajinović et al. 2011); this resulted in a total of 31 stars being selected. We then ran pPXF over all binned spectra, with ionised gas emission regions (H β , [OIII] and [NI]) masked out. We allowed for ten additive Legendre polynomials when performing the fits. We determined measurement errors by adding Gaussian noise to the spectra and rerunning the fits for 100 iterations each, with the pPXF penalty set to zero as prescribed in section 3.4 of Cappellari & Emsellem (2004). We present three example pPXF fits in Figure 2.

We are using deep spectroscopic observations that go well below the sky level; this means that our data will be dominated by systematics - such as imperfect sky subtraction and template mismatch - and that Monte-Carlo simulations will underestimate the true errors on the kinematics (Arnold et al. 2014). We therefore evaluated the systematic errors on our kinematics, by running pPXF for a second time, using stars from the MILES library of stars instead of ELODIE. The MILES library has an estimated resolution of 2.5\AA FWHM and so we broadened our spectra accordingly for this run. We selected a sample of MILES stars by fitting to elliptical annuli in the same manner as for the ELODIE stars, selecting 29 stars in total, and then we performed pPXF fits on all spectral bins. We show example fits with MILES in Figure 3 and we compare the ELODIE and MILES kinematics in Figure 4.

We find non-negligible offsets between our two runs for all four kinematic moments, suggesting the need to include systematic errors in our analysis. We estimated systematic errors of 4 km/s and 5 km/s for our velocity and dispersion, and we estimated systematic errors of 0.03 for h_3 and h_4 . We added these errors in quadrature to the initial error values. We found that a minority of kinematic values continued to exhibit large offsets relative to their errors once this process was completed; we masked the affected values from all subsequent analysis.

We present the resulting LOSVD maps in Figure 5 along with the associated errors. We find evidence of ordered rotation throughout the FOV. Figure 5 implies an anticorrelation between V/σ and h_3 , which may indicate

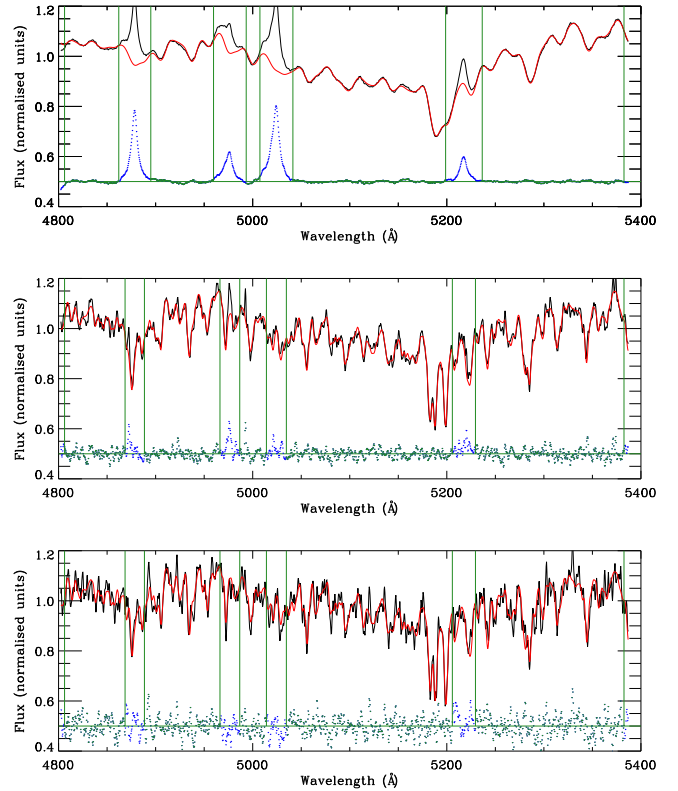


Figure 2. Example four-moment pPXF fits for the centremost fibre (top), a $2R_e$ spectral bin (middle) and a $3R_e$ spectral bin (bottom). Black lines show the normalised spectra and red lines the best fits. Vertical green lines indicate the positions of emission lines which we excluded from the fit. The blue line shows the residuals, with the horizontal green line marking the zero-point.

a rotating axisymmetric disc component within a slower-rotating bulge (e.g. Bender et al. 1994; Naab et al. 2014); this is expected for a fast-rotator like NGC 3998. Our kinematics extend beyond $3R_e$, and thus cover a significantly wider FOV than previous IFU observations of this galaxy. We find a peak velocity of 190 km/s and a peak velocity dispersion of 277 km/s.

3.2 SAURON Kinematics

To test the accuracy of our kinematic extraction, we compared our velocity dispersion results to those of the ATLAS^{3D} survey (Cappellari et al. 2011)¹ in the region where the datasets overlap. We mapped each of our fibres or spectral bins to the luminosity-weighted average of all enclosed SAURON pixels or bins, after realigning the datasets as explained in section 4.2. We show the results of this process in Figure 7. The ATLAS^{3D} velocity dispersions are noticeably higher at lower Mitchell dispersion values, but we note that all such offsets occur in regions where the ATLAS^{3D} data has been binned.

¹ Data available from <http://purl.org/atlas3d>

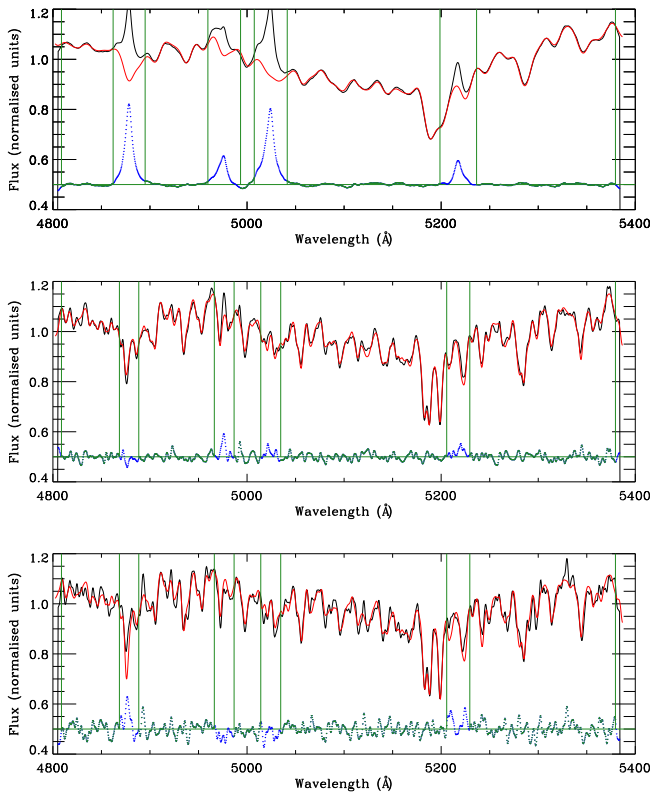


Figure 3. As in Figure 2, but using MILES stars as templates instead of ELODIE. The Mitchell spectra have been broadened to match the MILES resolution, as discussed in the text.

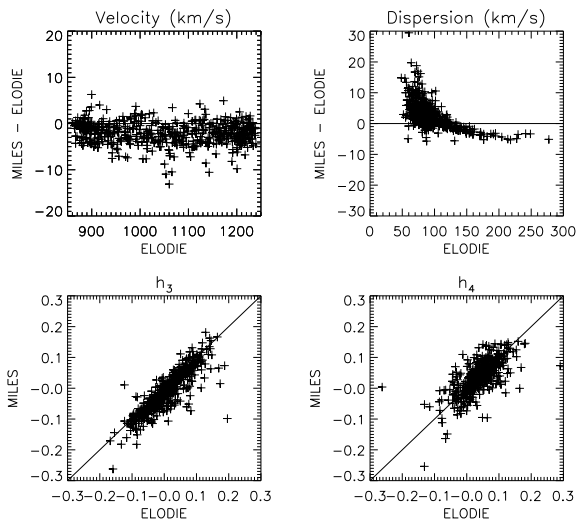


Figure 4. Comparison between kinematics calculated from Mitchell using ELODIE and MILES templates. We find non-negligible differences in the results, suggesting the need to consider systematic errors in our work.

There are a number of caveats concerning this comparison. Since the relative offsets are largest in the binned ATLAS^{3D} regions, it is possible that the offsets are due to S/N differences between the datasets (e.g. Arnold et al. 2014). The velocity resolution of the datasets are also very different: the ATLAS^{3D} data has an instrumental dispersion of 95 km/s (Cappellari et al. 2011), while the value for the finalised Mitchell spectra is 41 km/s. This could further increase dispersion offsets when the dispersion approaches the ATLAS^{3D} resolution. Differences in wavelength coverage are another consideration (Foster et al. 2016); however, we have verified that fitting only to the SAURON wavelength region does not significantly affect our kinematics (Figure 6). Lastly, the ATLAS^{3D} kinematics were extracted using the MILES library of observed stars (Sánchez-Blázquez et al. 2006), as opposed to the ELODIE library that we used.

We therefore re-extracted the NGC 3998 SAURON kinematics from the public SAURON datacubes². We used the ELODIE stellar templates as pPXF inputs, broadened to the SAURON spectral FWHM of 3.9 Å (Cappellari et al. 2011). We again allowed for a 10th-degree additive polynomial correction and allowed the stellar template to vary between bins, for maximum consistency with the Mitchell kinematics, and we used the same bin locations as in the published ATLAS^{3D} data. We derived errors in pPXF by adding noise to spectra as described previously, and we again calculated additional systematic errors by re-fitting with MILES templates. We noted large offsets in a handful of central pixels, which possibly relates to template mismatch from the central LINER region; we added corresponding systematic error terms to the affected pixels individually. Over the remaining field of view, we derived systematic error terms of 4 km/s and 0.03 for the velocity and h_3 terms respectively; we did not find it necessary to include systematic terms for the velocity dispersion or h_4 , though a small number of bad pixels were identified in the same manner as with the Mitchell data. We present the resulting LOSVD and error maps in Figure 8.

In Figure 9, we compare the dispersions from our Mitchell kinematics with those from the re-extracted SAURON results. Our own SAURON dispersions are generally slightly lower than reported in ATLAS^{3D}, but we continue to see some regions in the outskirts where the SAURON dispersions are higher than measured by the Mitchell. Overall, we find our kinematics to be slightly offset with respect to ATLAS^{3D}.

We use our own SAURON kinematics in all subsequent analysis, in order for all of our data to have been extracted from the same stellar library for maximum consistency.

4 DYNAMICAL MODELLING

We generated a series of orbit-based models of NGC 3998 using the Schwarzschild orbit superposition method (Schwarzschild 1979). We employed the method and code

² Available from <http://purl.org/atlas3d>

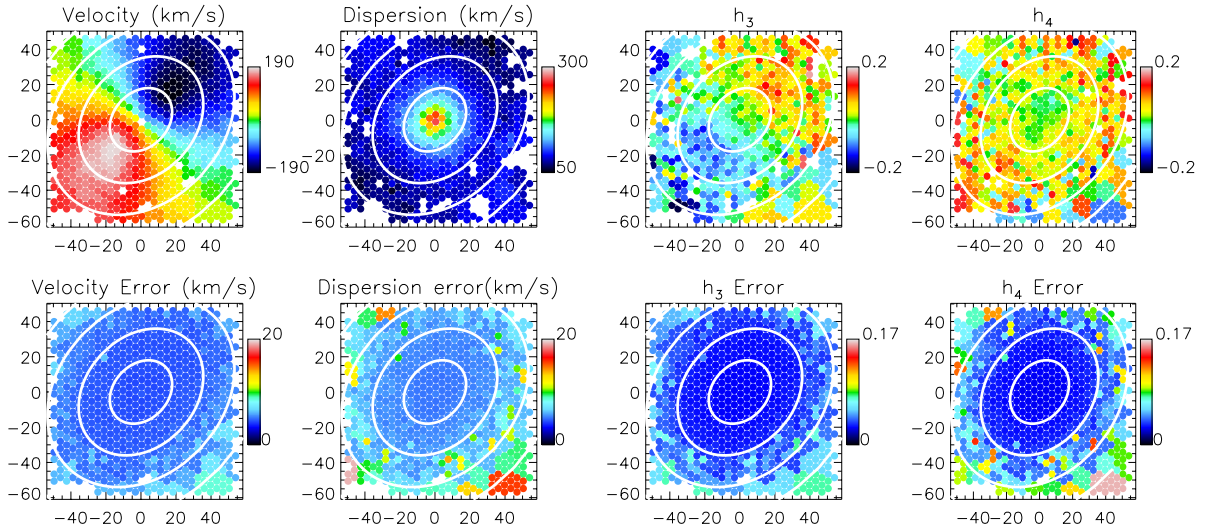


Figure 5. LOSVD and error maps measured for four moments from Mitchell Spectrograph data. The white contours are spaced in units of effective radii. We find evidence of ordered rotation through the FOV, with h_3 taking the opposite sign to the velocity. White regions show bins/fibres that were excluded, as discussed in the text.

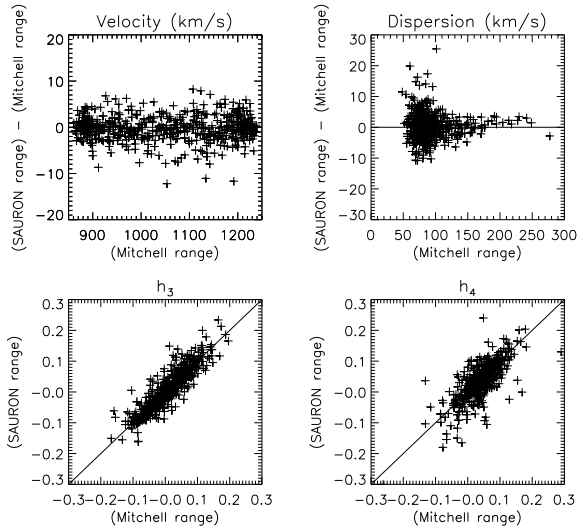


Figure 6. Comparison between kinematics calculated when fitting Mitchell spectra with ELODIE stars over the full available wavelength range vs kinematics calculated over the SAURON wavelength range. Black lines mark the 1-1 relation. We find that the wavelength range has little overall effect, with the scatter effectively captured by our derived uncertainties.

of [van den Bosch et al. \(2008\)](#), which allows for triaxial geometries and has previously been shown to accurately reproduce simulated ETGs ([van de Ven et al. 2008](#); [van den Bosch & van de Ven 2009](#)). For a full description we refer the reader to [van den Bosch et al. \(2008\)](#), but we provide a brief overview in section 4.1 along with details of our implementation. We describe the calculation of the spatial PSF in section 4.2.

4.1 Method Overview

First, we construct a gravitational potential using a supplied galaxy surface brightness distribution, a supplied set of viewing angles and a supplied set of dark halo parameters. We construct an orbit library as follows. We first sample orbits along 21 equipotential shells logarithmically spaced between $0.5''$ and $294''$, and we sample over 7 radial and 7 angular directions for each shell. We then calculate an additional sets of orbits by dropping stars from successive equipotential curves, in order to ensure enough box orbits in our library over the galaxy’s outer regions; these orbits are sampled along the same 21 equipotential shells and along 7×7 directions spaced evenly in terms of angles. We bundle together 3^3 orbits with adjacent starting positions, producing a library of 18520 orbits overall. We then determine the superposition of orbits that best fits the kinematics using a quadratic programming method to solve the least-squares problem. The size and shape of individual spectral bins is accounted for when fitting to the kinematics.

We parametrise the surface brightness using the Multi-Gaussian Expansion (MGE) method of [Emsellem et al. \(1994\)](#), which is implemented in the code of [Cappellari \(2002\)](#). The MGE method models an observed surface brightness distribution as a set of two-dimensional Gaussian components, each of which may have unique peak values, widths and axial ratios. By deprojecting the galaxy for a set of viewing angles and assuming a constant mass-to-light (M/L) ratio, one can therefore obtain a density profile for the galaxy’s visible component. For NGC 3998, we used the published I-band MGE model of [Walsh et al. \(2012\)](#), which was generated by combining *HST* Wide-Field-Camera 2 (WFC2) imaging in the center with wide-field imaging from the Wide-Field InfraRed Camera (WIRCAM) on the Canadian-French Hawaiian telescope. The model is well-resolved in the centre and ex-

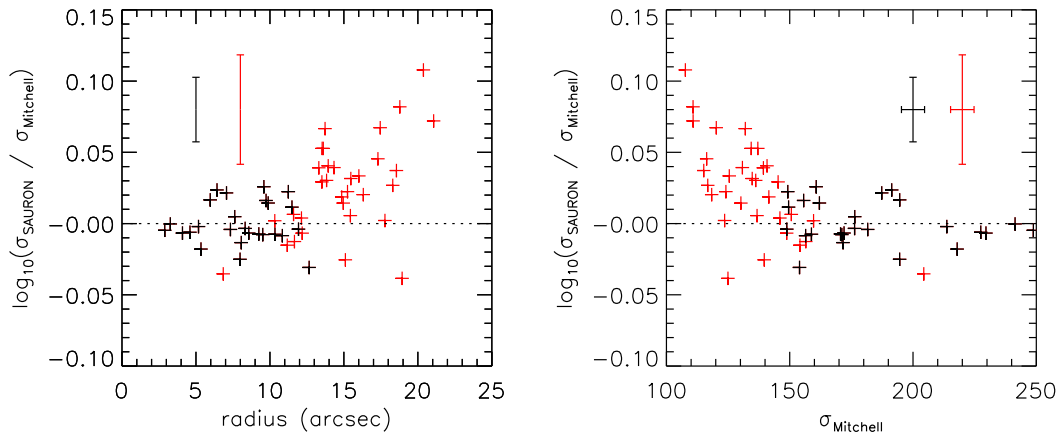


Figure 7. Left: ratio of ATLAS^{3D} to Mitchell Spectrograph velocity dispersions, plotted against radius (left) and the Mitchell velocity dispersion (right). The ATLAS^{3D} values are given as the flux-weighted averages of all values within a given Mitchell fibre. Black crosses on the left plot represent regions where no voronoi-binning took place, while red crosses indicate where the ATLAS^{3D} results were binned. We show representative error bars on both plots. We observe notable offsets at low Mitchell dispersions, where the ATLAS^{3D} spectra were binned.

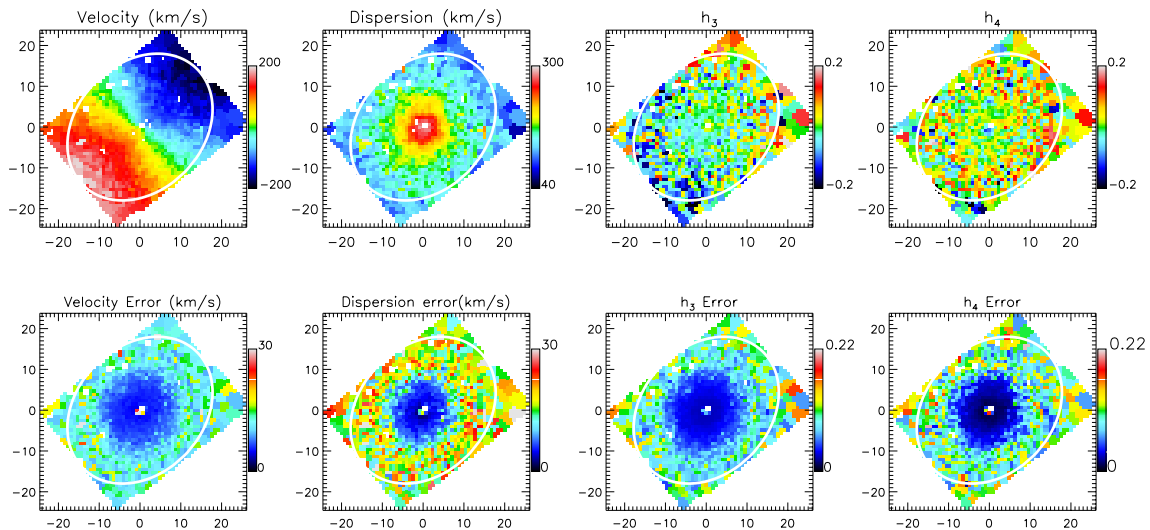


Figure 8. LOSVD and error maps that we re-measured from SAURON data, with the ELODIE library employed instead of the MILES library used in ATLAS^{3D}. The white ellipse shows the region enclosed by the innermost effective radius. Excluded datapoints are shown as white spaces.

tends well beyond three effective radii. This MGE model has a photometric position angle (PA) of -41.5° ; this is slightly misaligned with our kinematic PA of -44° , inferred from the method described in Appendix C of [Krajinović et al. \(2006\)](#).

We parametrise the viewing angle using the three triaxial shape parameters (q, p, u) , which can be related to the viewing angles $(\vartheta, \varphi, \psi)$ using equation (10) in [van den Bosch et al. \(2008\)](#). In qualitative terms, q represents the short-to-long axis ratio, p the intermediate-to-long axis ratio, and u the ratio between the projected and intrinsic MGE Gaussian widths along the galaxy ma-

ajor axis. For an axisymmetric galaxy, p and u are both equal to unity and q is the only free shape parameter; in this case, q is directly related to the galaxy viewing angle or inclination. All three values correspond to the *flattest* input Gaussian ($q' = 0.756$) of the input MGE surface brightness model; every MGE Gaussian component has a different projected axial ratio, and so will have different triaxial shape parameters at a given assumed viewing angle.

We used kinematics from both the Mitchell Spectrograph and SAURON to fit the models. We masked Mitchell fibres with centres less than $8''$ from the galaxy

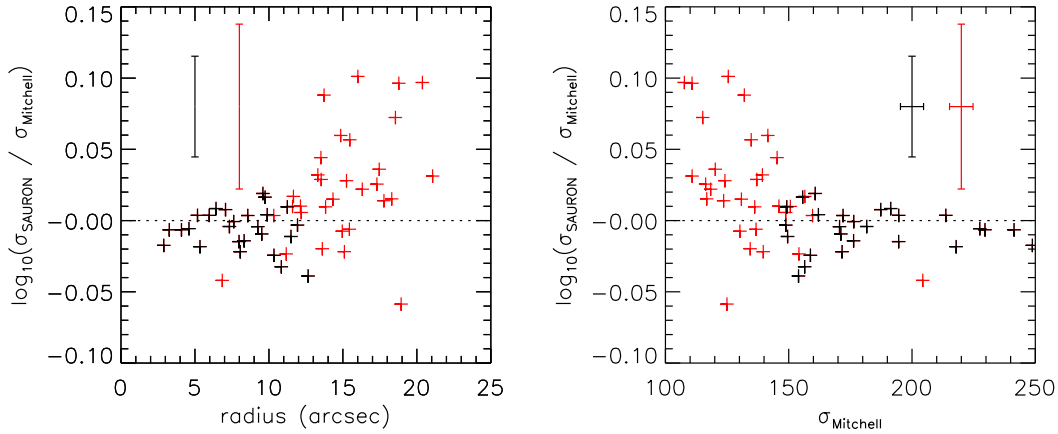


Figure 9. Ratio of the re-extracted SAURON velocity dispersions to those of Mitchell Spectrograph velocity dispersions, plotted against radius (left) and Mitchell dispersion (right). Lines and symbols are as in Figure 7. We find very little overall offset in unbinned SAURON regions, but once again see a number of large offsets where binning in the SAURON data becomes important.

centre and we masked SAURON pixels greater than $10''$; this lets us combine the wide FOV of the Mitchell data with the higher spatial resolution of the central SAURON data, while limiting the overlap between datasets to avoid the fit being unfairly dominated by the galaxy centre. We brought the central values of the velocity and h_3 data to zero using the methods of Krajnović et al. (2006) and van den Bosch & de Zeeuw (2010) respectively, which both calculate systemic components in the data as part of their routines.

We obtain the best-fitting superposition of orbits for each model using a quadratic programming solver (Gould et al. 2003). We fit the orbits to our kinematics, with the intrinsic and projected model masses constrained to be within 2% of the supplied MGE model at all times. We parametrise the quality of each fit using the χ^2 statistic, which we define as

$$\chi^2 = \sum_{i=1}^N \left(\frac{D_{mod,i} - D_i}{\Delta D_i} \right)^2 \quad (2)$$

where D signifies the values for each kinematic moment in turn, with D_{mod} the values from a given model.

We set all confidence intervals using the expected standard deviation of the χ^2 statistic, $\sqrt{2N_{obs}}$, where N_{obs} is the total number of observables used to constrain the model parameters. This approach was first introduced in van den Bosch et al. (2008) and has since been validated in both van de Ven et al. (2008) and van den Bosch & van de Ven (2009). It is preferable to using traditional sigma confidence intervals when N_{obs} is large, as it better captures the uncertainties associated with the χ^2 statistic itself. Here, $N_{obs} = 3866$ and so we define our confidence intervals using $\Delta\chi^2 = 87.9$. For comparison, the 3σ confidence interval for four free parameters would be $\Delta\chi^2 = 16.25$.

We include a dark matter mass distribution by as-

suming a spherical NFW dark halo (Navarro et al. 1996), in which the dark halo density profile is given as

$$\frac{\rho(r)}{\rho_{crit}} = \frac{\delta_c}{(r/r_s)(1+r/r_s)^2} \quad (3)$$

where $r_s = r_{200}/c$ is a characteristic break radius and $\rho_{crit} = 3H^2/8\pi G$ is the critical density of the universe. c is the concentration parameter, while δ_c is the characteristic overdensity. This halo therefore has two free parameters: the concentration, and the halo mass $M_{200} = 200(4\pi/3)\rho_{200}^3$. For the rest of this paper, we parametrise the halo mass in terms of M_{200}/M_* , where M_* represents the stellar mass component of NGC 3998.

4.2 PSF determination

It is non-trivial to determine the PSF of our Mitchell observations, due to both the large individual optical fibres and the high number of individual datacubes that were combined during the data reduction process. We therefore elected to use the method of (Krajnović et al. 2009): a provided surface brightness model is convolved with a proposed PSF and then compared to an observed flux map, in order to optimise both the PSF parameters and the galaxy central position.

The models of van den Bosch et al. (2008) code parametrize the PSF as the sum of one or more Gaussian PSF components. We experimented with including two components, but found only one of these components to produce a non-negligible contributions; as such, we ultimately allowed for only a single Gaussian PSF component in the model. We allowed the position of the galaxy center to vary, and further allowed for a non-zero sky brightness to account for any residual sky contamination, producing four free parameters overall. We varied these parameters to determine the best-fitting spatial PSF and galaxy center, in each case convolving our MGE model with a given PSF Gaussian, and found a best-fit PSF of $\sigma = 1.40''$.

We also fitted a two-component PSF to the SAURON datacubes. The SAURON data cubes are reported to be positioned such that the galaxy nucleus is placed precisely on the IFU lenslets. We verified this by first letting the RA and DEC positions of the galaxy vary as before; we found both best-fitting values to be $< 0.1''$ away from the stated numbers, and so we fitted a second time with the centre fixed to the ATLAS^{3D} position. Our best-fit PSF Gaussians have dispersions of $\sigma = 0.49''$ and $\sigma = 1.04''$ with relative weights of 0.7 and 0.3; since both Gaussians have non-negligible weights and imply the existence of extended PSF wings, we refrain from fitting the SAURON PSF with a single Gaussian component.

5 RESULTS

It is computationally expensive to fit for both the galaxy viewing angle and dark matter parameters simultaneously, due to the large number of free parameters involved. We therefore began by estimating a reasonable set of NFW parameters for which to fit the stellar M/L and galaxy shape. We used the MGE model and best-fit M/L result of Walsh et al. (2012) to derive a galaxy stellar mass of $7 \times 10^{10} M_{\odot}$, and we then estimated a dark-to-stellar mass fraction of 34.8 using the lowest-redshift fitting formula of Leauthaud et al. (2012). We then used the implied dark halo mass of $2.434 \times 10^{12} M_{\odot}$ to estimate an NFW concentration of $\log(c) = 0.867$ using the formula of Sánchez-Conde & Prada (2014).

We then generated a grid of triaxial orbit models which sampled the shape parameters (q, p, u) (for the *flat-test* MGE Gaussian component) and the stellar M/L. We sampled q down to a low minimum value of 0.06, motivated by the FR shape results of Weijmans et al. (2014), and we sampled p down to a value of 0.92. We used all possible values of u , as limited by the values of q and p (see, e.g., van den Bosch et al. 2008, for an explanation). We sampled 16 I-band stellar M/L values evenly between 3.1 and 6.1. We found a galaxy shape of $(q, p, u) = (0.06_{-0.00}^{+0.18}, 0.98_{0.004}^{+0.003}, 0.99_{-0.001}^{+0.002})$. The lower bound on q corresponds to the lowest tested value and so is not a true lower limit. The narrow bounds on p and u are due the small misalignment between the photometric and kinematic PAs discussed previously, which produces a kinematic misalignment between models and data (and so a large χ^2 increase) unless p and u take very specific values.

The shape parameters (q, p, u) correspond to the *flat-test* component of the input MGE model. We calculate the resulting shape of the overall model by first deprojecting it according to (q, p, u) and then fitting spheroids of constant luminosity density. We thus find a minor-to-major axis ratio at $1R_e$ of $q_{R_e} = 0.44_{-0.00}^{+0.05}$. We conclude from this that NGC 3998 is a flattened and near-oblate galaxy.

We next generated a series of models in which we fitted for the NFW dark halo mass, the stellar M/L and the axis ratio q . We fixed p and u to values of 0.98 and 0.99 respectively, as per the discussion on the previous paragraph. We used q values between 0.06 and 0.38, in steps of 0.08, to ensure that all reasonable q values were covered given the results of the previous model grid. We fixed the

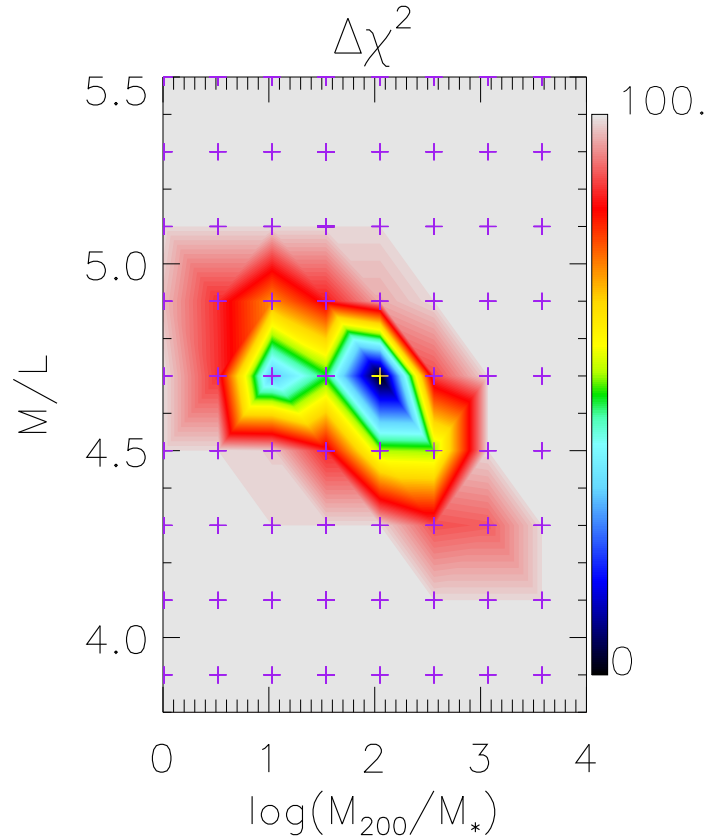


Figure 10. Map of $\Delta(\chi^2)$ in terms of the dark matter mass fraction and the stellar M/L, with the axis ratio q marginalised over. The yellow point represents the best-fitting model.

halo concentration c to the same value as before; this is because the NFW scale radius will be significantly beyond our FOV for most reasonable halo parameters, making the dark mass and concentration highly degenerate (see, e.g. Yıldırım et al. 2016, for a similar argument). We used a range of $\log_{10}(M_{200}/M_*)$ from 0.01 to 4.09, with models without dark matter also included. We sampled the same M/L values as before.

We present the $\Delta\chi^2$ for the above-described model in terms of M_{200} , M/L in Figure 10, in which the galaxy shape has been marginalised over, and we present separate $\Delta\chi^2$ profiles for M_{200} , M/L and q_{lum} in Figure 11. Our best-fit model has a χ^2/DOF of 1.11. We find $M/L = 4.7_{-0.45}^{+0.32}$, with a dark halo mass $\log_{10}(M_{200}/M_*) \leq 3.13$. We find no firm lower limit on the dark halo mass, as the best-fitting DM-free case falls within our χ^2 confidence limit.

Marginalising over M/L and the dark matter mass, we find $q_{R_e} = 0.44_{-0.00}^{+0.05}$, where the minimum is again set by the limits of our sampling; this corresponds to an upper limit of 42.5° on the viewing angle θ . If we instead consider models with no dark matter only, we find $q_{R_e} = 0.48_{-0.04}^{+0.04}$ ($\theta < 43.4^\circ$). Thus, the q_{R_e} confidence region shows a slight dependence on the presence of dark matter, with the best fit q_{R_e} value higher in the DM-free case.

In Figure 12 we plot the inferred best-fit dark matter fraction along with the associated confidence interval. We define the dark matter fraction as the fraction of

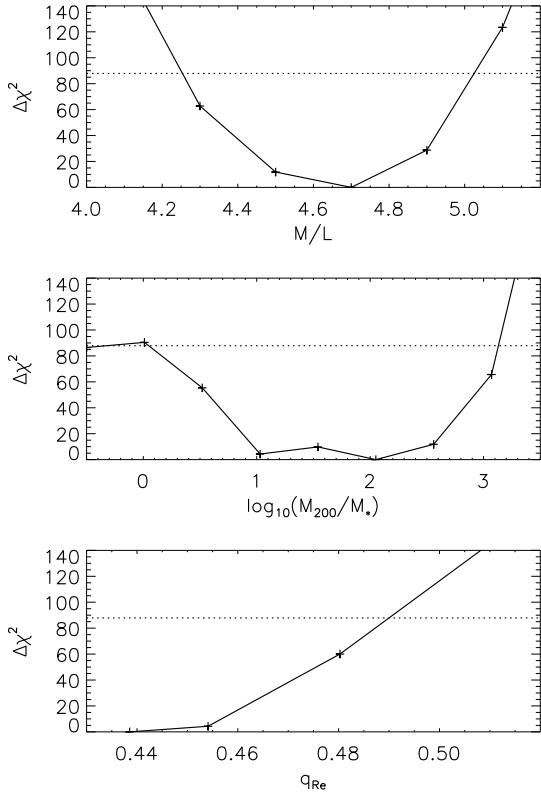


Figure 11. $\Delta\chi^2$ plotted as a function of the I-band M/L (top), the NFW dark halo mass (middle) and the axial ratio q_{R_e} , with all other parameters marginalised over in each case. The left-most point on the middle window is for the DM-free case. The horizontal dashed line signifies $\Delta\chi^2 = 87.9$, which marks the bounds of our confidence region and is set by the standard deviation of the χ^2 statistic. We obtain relatively tight constraints on the stellar M/L and we obtain tight upper limits on q_{R_e} and the dark halo mass.

dark mass within a sphere of given radius, using a circularised MGE surface brightness model. We find a best-fitting dark matter fraction of $(7.1^{+8.1}_{-7.1})\%$ within $1R_{e,circ}$, where $R_{e,circ}$ is the circularised effective radius of $23.99''$ reported in table 1 of Cappellari et al. (2013a), which is in agreement with the dark fraction of $(15 \pm 6)\%$ reported in Cappellari et al. (2013b). Thus, we find that low dark mass fractions are preferred by our models.

6 DISCUSSION

In the previous section, we derived best-fit parameter ranges for NGC 3998’s shape, I-band stellar M/L, and NFW dark halo parameters. We found NGC 3998 to be a near-oblate, face-on fast rotator, in agreement with the flattening inferred for this galaxy in Cappellari et al. (2013a). We obtain tight constraints on the intrinsic galaxy shape, unlike in Walsh et al. (2012). Our best-fit I-band M/L is also somewhat lower than reported in Walsh et al. (2012), though it is consistent within the errors. The latter point can immediately be understood as

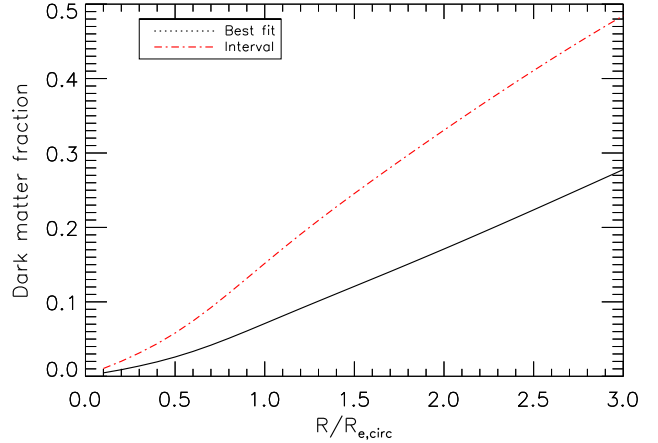


Figure 12. Profile of best-fit enclosed dark mass fraction out to $3R_{e,circ}$ (black line), along with the upper limit (dash-dotted red line). We show no lower limit because our best-fit DM-free model falls within our χ^2 confidence limit. $R_{e,circ}$ is the circularised effective radius from table 1 of Cappellari et al. (2013a). We find tight upper limits on the dark matter content, with the models preferring little dark matter within $1R_{e,circ}$.

the consequence of including a dark halo, while the use of a wide two-dimensional field-of-view enables significantly tighter constraints on the shape parameters than was previously possible. We find an axial ratio $q_{R_e} = 0.44^{+0.05}_{-0.00}$ from our models, which corresponds to a viewing angle θ lesser than 42.5° ; this is consistent with the inclination of $(38 \pm 5)^\circ$ reported in Cappellari et al. (2013a).

Our $1R_{e,circ}$ dark matter fraction of $(7.1^{+8.1}_{-7.1})\%$ is lower than commonly reported for ETGs from simulations or observations (e.g. Weijmans et al. 2009; Barnabè et al. 2011; Remus et al. 2013; Wu et al. 2014), but is consistent with the fraction of $(15 \pm 6)\%$ reported in Cappellari et al. (2013b) and is also well within the scatter of low dark fractions reported by Cappellari et al. (2013a). We note that the inferred stellar mass for NGC 3998 is close to the $M_* - M_{halo}$ pivot mass of $4.5 \times 10^{10} M_\odot$ inferred from weak lensing studies of nearby galaxies (Leauthaud et al. 2012), meaning that a lower-than-average dark mass fraction is perhaps not surprising.

Cappellari et al. (2013b) report an r-band M/L of 6.58 ± 0.39 for this galaxy, from stellar population modelling assuming a Salpeter IMF slope. We convert this to an I-band M/L of 4.72 ± 0.28 using

$$(M/L)_I = (M/L)_r \times 10^{\frac{(I-r)_{gal} - (I-r)_\odot}{2.5}} \quad (4)$$

where we obtain a galaxy color $(I-r)_{gal}$ of -0.48 by comparing the Walsh et al. (2012) MGE model with the r-band MGE model from ATLAS^{3D} (Scott et al. 2013) out to $50''$, and where we assume a Sun color of $(I-r)_\odot = -0.12$ (and references therein Blanton & Roweis 2007). Our I-band M/L of $4.7^{+0.32}_{-0.45}$ inferred from Schwarzschild modelling is therefore in excellent agreement with the Cappellari et al. (2013b) stellar population models. For models without dark matter, we find an I-band M/L of $4.9^{+0.27}_{-0.25}$, which is also within the uncertainty of the Cappellari et al. (2013b) value. Thus, we find

Model	q	M/L	$\log_{10}\left(\frac{M_{200}}{M_*}\right)$	$f_{DM}(R_{e,circ})$
Best fit	0.06	4.7	2.05	7.1%
DM-heavy	0.06	4.1	3.58	20.2%
DM-free	0.22	4.9	N/A	0%

Table 2. Summary of the three models shown in Figures 13–16 and discussed in the text. $f_{DM}(R_{e,circ})$ denotes the dark fraction within one (circularised) effective radius.

that the Cappellari et al. (2013b) models are consistent with a low dark fraction for this galaxy.

In Figure 13 and Figure 14, we compare our input Mitchell kinematics maps to three of our orbit models: our best-fit model, a dark matter heavy model and our best-fitting dark-matter-free model. We show the same comparisons for the SAURON data in Figure 15 and Figure 16. We summarise the properties of the selected models in Table 2. The DM-free model is within our χ^2 confidence criterion, while the DM-heavy model is significantly beyond it ($\chi^2 - \chi_{lim}^2 = 164.1$). The DM-free model looks very similar to the overall best-fit model, which is unsurprising given the low dark matter content that we infer. The DM-heavy model also looks similar over most of the FOV, though its velocity dispersions are generally somewhat higher in the outskirts than for the best-fit model (Figure 17); this is the main cause of the χ^2 difference between the two models.

We have seen above that higher dispersion values in the outskirts correspond to larger dark matter fractions. Were our dispersions to be underestimated, then this could bias our results towards lower dark matter fractions. We discussed the robustness of our kinematics in section 3, during which we noted that our Mitchell velocity dispersions are somewhat lower away from the centre than would be implied from ATLAS^{3D}. However, we found good agreement in the two instruments’ dispersions within the *unbinned* ATLAS3D region, and we have also verified that fitting Mitchell data with MILES does not significantly affect the inferred offset between the instruments. We also note that pPXF fits with MILES produce somewhat higher dispersions in the outskirts of the Mitchell data than fits with ELODIE, with a median 7.8% difference for ELODIE dispersions below 70 km/s; however, this is approaching the intrinsic resolution of the MILES library (60 km/s) and so we view the ELODIE kinematics as more reliable over this region. Since our dark matter fraction is consistent with the ATLAS^{3D} value, we do not explore this point further.

In Figure 18, we plot the total (dark plus baryonic) mass density profiles of all allowed Schwarzschild models. We find the models to follow near-isothermal profiles beyond the central effective radius, in good agreement with the average logarithmic slope of 2.19 ± 0.03 reported from the dynamical models of Cappellari et al. (2015). The density slopes within the central effective radius are somewhat steeper, and resemble the stars-only density profiles of that same paper; this is unsurprising, given the low

central dark matter fractions of all our allowed models.

In Figure 19 we present the distribution of orbits in our best-fitting orbit model as a function of spin parameter λ_z and position. We find evidence of both a slow-rotating bulge component and a fast-rotating disc, with the disc becoming increasingly dominant beyond the central half-light radius. We also find a non-negligible counter-rotating component within the central 10 arcseconds, which is not visible in the SAURON or Mitchell kinematics maps. Within $1R_e$, we find the orbital distribution to consist of 61.3% prograde orbits, 26.1% non-rotating ($\lambda_z < 0.2$) orbits and 12.6% retrograde orbits; within $3R_e$, we find 70.5% prograde orbits, 19.5% non-rotating orbits and 10.0% retrograde orbits. We show the distribution of orbits for the selected DM-free model in Figure 20; we find that the distribution is qualitatively similar to that seen in Figure 19, with a bulge and disc component present along with a non-negligible counter-rotating component. We find counter-rotating components of similar mass fraction to be present in all models allowed by our χ^2 criterion; as such, this appears to be a necessary component to successful model fits. Overall, these figures provide an excellent illustration of how multiple datasets may be employed to study an object in detail.

In Figure 21 we plot the orbital anisotropy parameters $\beta_r = 1 - (\sigma_t/\sigma_r)^2$ and $\beta_z = 1 - (\sigma_z/\sigma_R)^2$ as a function of radius, as inferred from our best-fit model. We define the tangential velocity dispersion σ_t as $\sigma_t^2 = (\sigma_\theta^2 + \sigma_\phi^2)/2$, where (r, θ, ϕ) are the standard spherical coordinates. (R, z) are cylindrical coordinates, with σ_z therefore denoting the dispersion out of the plane of the disc. We find our best-fit model to be radially anisotropic ($\beta_r > 0$) in the centre, similar to the results of Walsh et al. (2012), and we find tangential anisotropy further out; this can be understood as a result of the bulge-disc separation discussed above. We find β_z to vary strongly as a function of position; this is different from the assumption of constant β_z employed in the axisymmetric jeans models of Cappellari et al. (2013b), even within the region covered by SAURON data.

An important caveat here is that the low inclination of the galaxy introduces a significant degeneracy in the MGE deprojection, as small changes to the (projected) MGE surface brightness model could potentially produce large changes in the deprojected mass distribution. Such changes would affect the inferred extent and flattening of individual galaxy components. Since rounder galaxy models are known to produce more radial anisotropies (e.g. Magorrian & Ballantyne 2001; Cappellari 2008), changes to individual components can be expected to affect the anisotropy similarly; this, then, is an alternative explanation for our finding of strong tangential anisotropy. A similar analysis on the outskirts of more edge-on galaxies would be revealing in this regard.

From the above discussion, our modelling implies NGC 3998 to be disc-dominated over much of the Mitchell FOV with only a small proportion of radial orbits in the outskirts. Late-time accretion of stars is expected from simulations to produce an excess of radial orbits beyond the central effective radius (e.g. Oser et al. 2010; Wu et al.

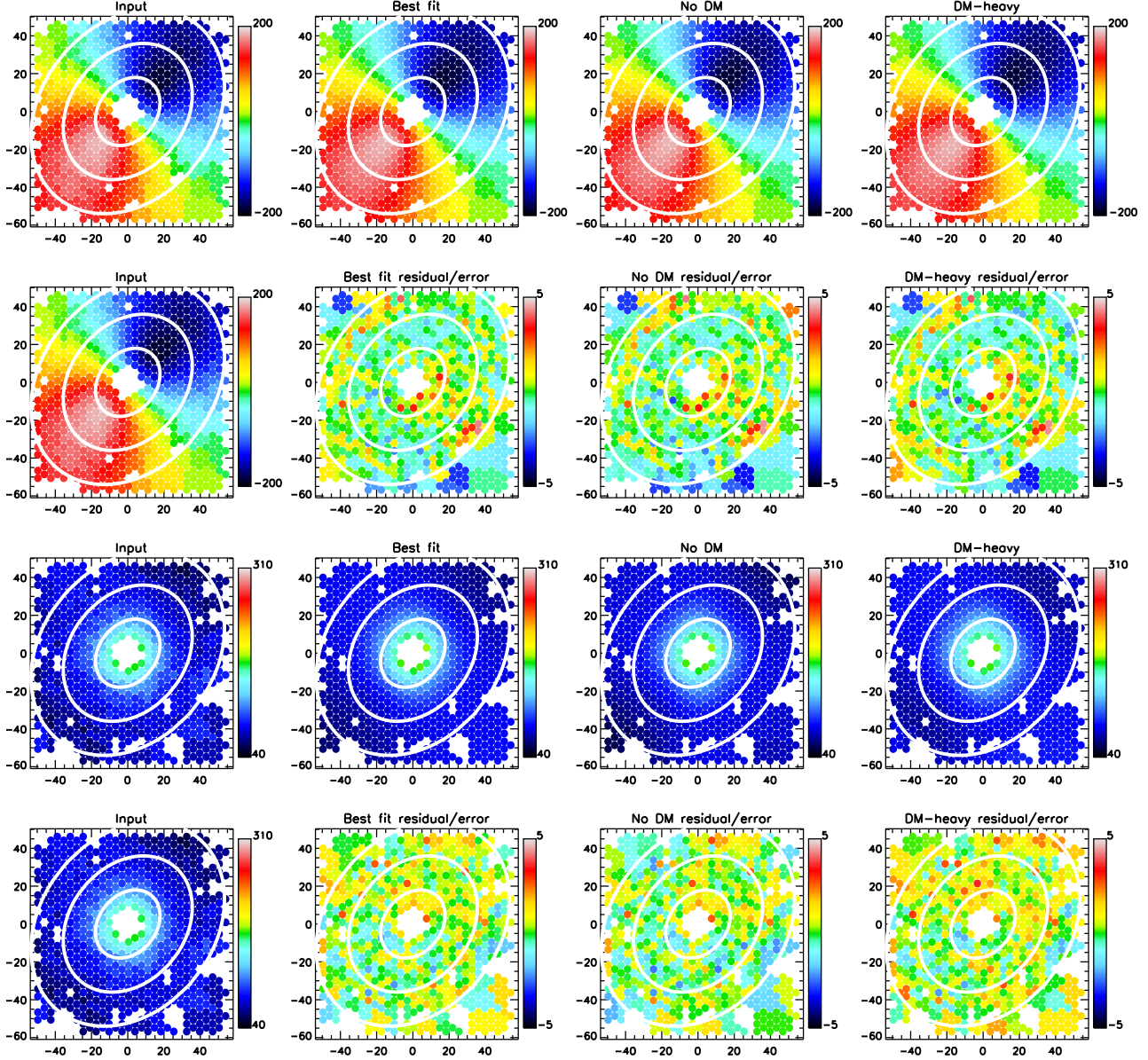


Figure 13. From top to bottom: input Mitchell velocity and model velocities, (model - data) velocity residual/error, input and model dispersions and (model - data) dispersion. We summarise the properties of the three selected models in Table 2. Only unmasked bins are shown.

2014), while tangential anisotropy is only observed in simulated galaxies with large fractions of in-situ formed stars (Wu et al. 2014); we therefore infer that late-time accretion did *not* play a major role in this galaxy, in agreement with the proposed FR formation path of Cappellari (2013) (in which only SRs have experienced late dry accretion). Simulations further suggest tangential anisotropy to indicate galaxies which have experienced a recent ($z < 2$) dissipational event (Röttgers et al. 2014), with the tangential anisotropy a result of the large fraction of in-situ formed stars. Our inferred galaxy shape of $q_{R_e} = 0.44^{+0.05}_{-0.00}$ is also consistent with a past dissipational event, from the cosmological simulations of Naab et al. (2014).

Overall, our models support the FR formation pic-

ture presented in Cappellari (2013). Our models imply little late-time accretion for this galaxy, which disfavors the two-phase evolutionary history associated with SRs. Our models are, however, consistent with some past dissipational event having occurred. Given the apparent lack of late-time accretion, we would not expect to find multiple components to this galaxy's stellar population; rather, we predict this galaxy to be dominated by an old population of internal origin. Such a prediction is also supported by the simple stellar population modelling of McDermid et al. (2015), who report an old (11.27 ± 1.95) stellar population of near-solar metallicity ($[Z/H] = -0.04 \pm 0.05$) from simple stellar population fits to the central effective radius.

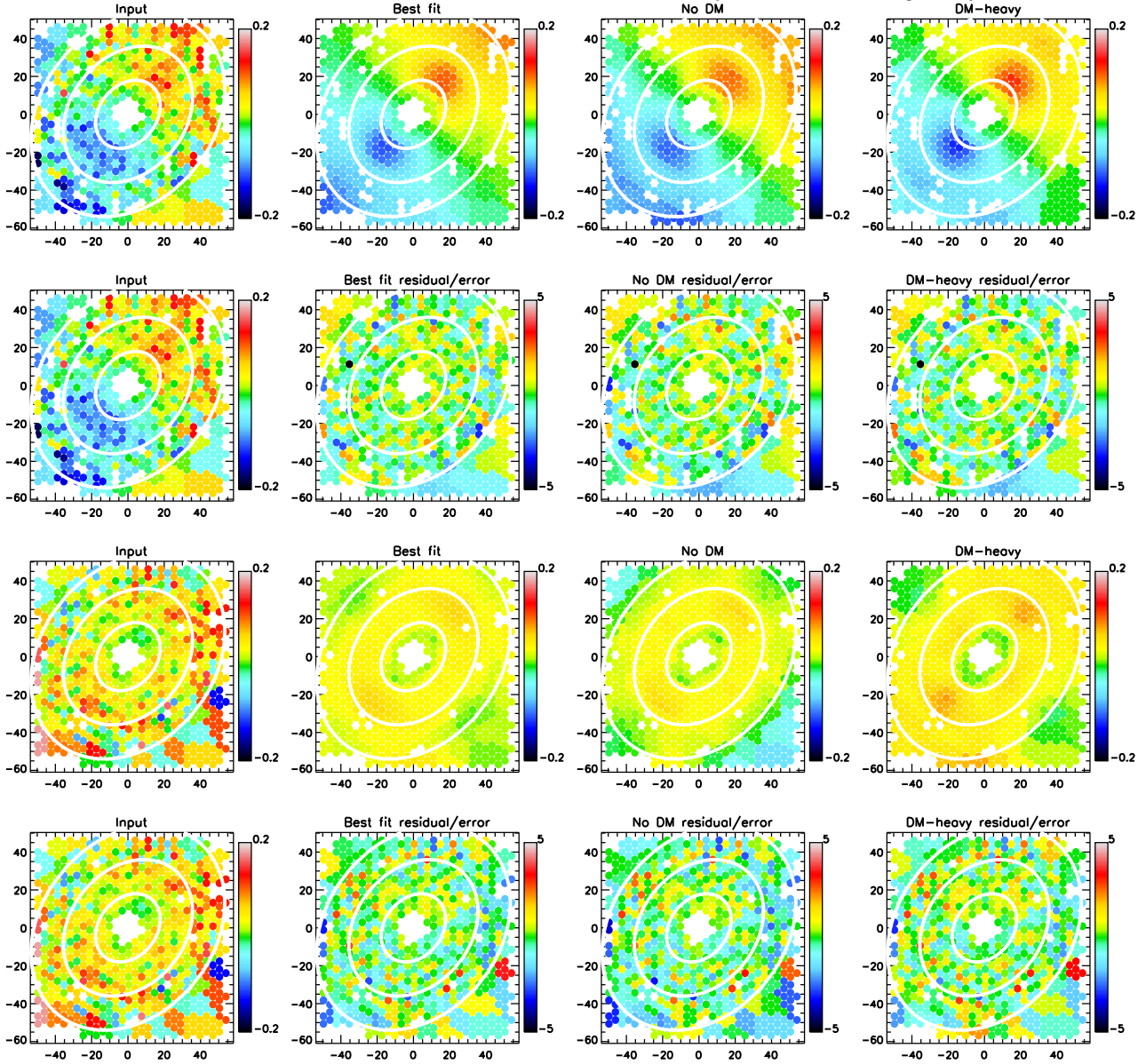


Figure 14. As in Figure 13, but for h_3 and h_4 .

7 SUMMARY AND CONCLUSION

We have presented an orbit-modelling analysis of the lenticular galaxy NGC 3998, with kinematics obtained from both Mitchell Spectrograph observations as well as from archival SAURON observations taken as part of ATLAS^{3D}. Our modelling implies NGC 3998 to be a near-oblate and flattened galaxy, consistent with the inclination reported in Cappellari et al. (2013a).

We find a small dark matter component to be preferred by our models. We obtain a dark matter fraction of $(7.1^{+8.1}_{-7.1})\%$ within the central (circularised) effective radius, which is lower than commonly reported for ETGs but which is consistent with the $(15 \pm 6)\%$ previously reported for this galaxy from ATLAS^{3D} data. We also find our I-band M/L results to be in excellent agreement

with previous ATLAS^{3D} spectral modelling results for this galaxy, which adds weight to the idea of there being little dark matter in this system within the observed stellar region.

We find NGC 3998 to be disc-dominated in its outer regions, with few radial orbits. We also find the orbital anisotropy to vary strongly as a function of position, with strong tangential anisotropy in the outskirts. From comparisons to simulations, we infer from both points that NGC 3998 has *not* experienced significant late-time accretion of stars. We also reason from our models that some past dissipational event could have occurred. Our modelling is therefore in good agreement with the proposed FR formation path of the ATLAS^{3D} collaboration, in which FRs form from the quenching of high-redshift spirals.

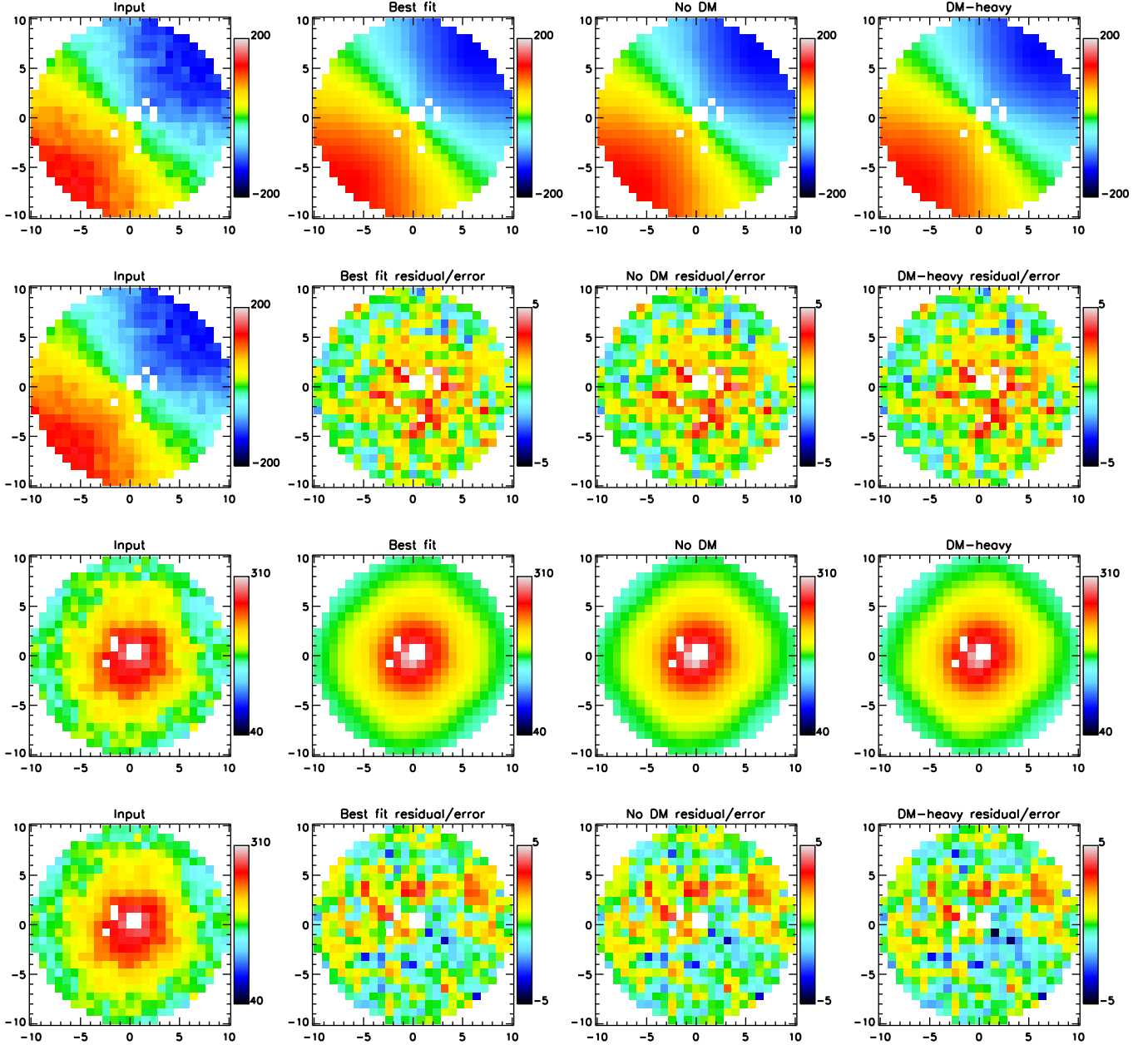


Figure 15. As in Figure 13, but for the SAURON data.

Overall, our results demonstrate the power of wide-field IFU instruments in studying a range of galaxy properties. We will perform a similar analysis on a wider sample in a future work.

ACKNOWLEDGEMENTS

We wish to thank the anonymous referee for their helpful and informative report which served to greatly improve the quality of the paper. We thank Josh Adams, Guillermo Blanc and Jeremy Murphy for their help with the data reduction. We thank Kevin Luecke for his help

with observing and we thank the staff of McDonald Observatory for their support. We thank Ronald Laesker for his insightful comments on comparing the SAURON and Mitchell kinematics. NFB was supported by STFC grant ST/K502339/1 during the course of this work. NFB acknowledges support from the Max Planck Institute for Astronomy in Heidelberg, Germany. AW acknowledges support from a Leverhulme Early Career Fellowship. MC acknowledges support from a Royal Society University Research Fellowship

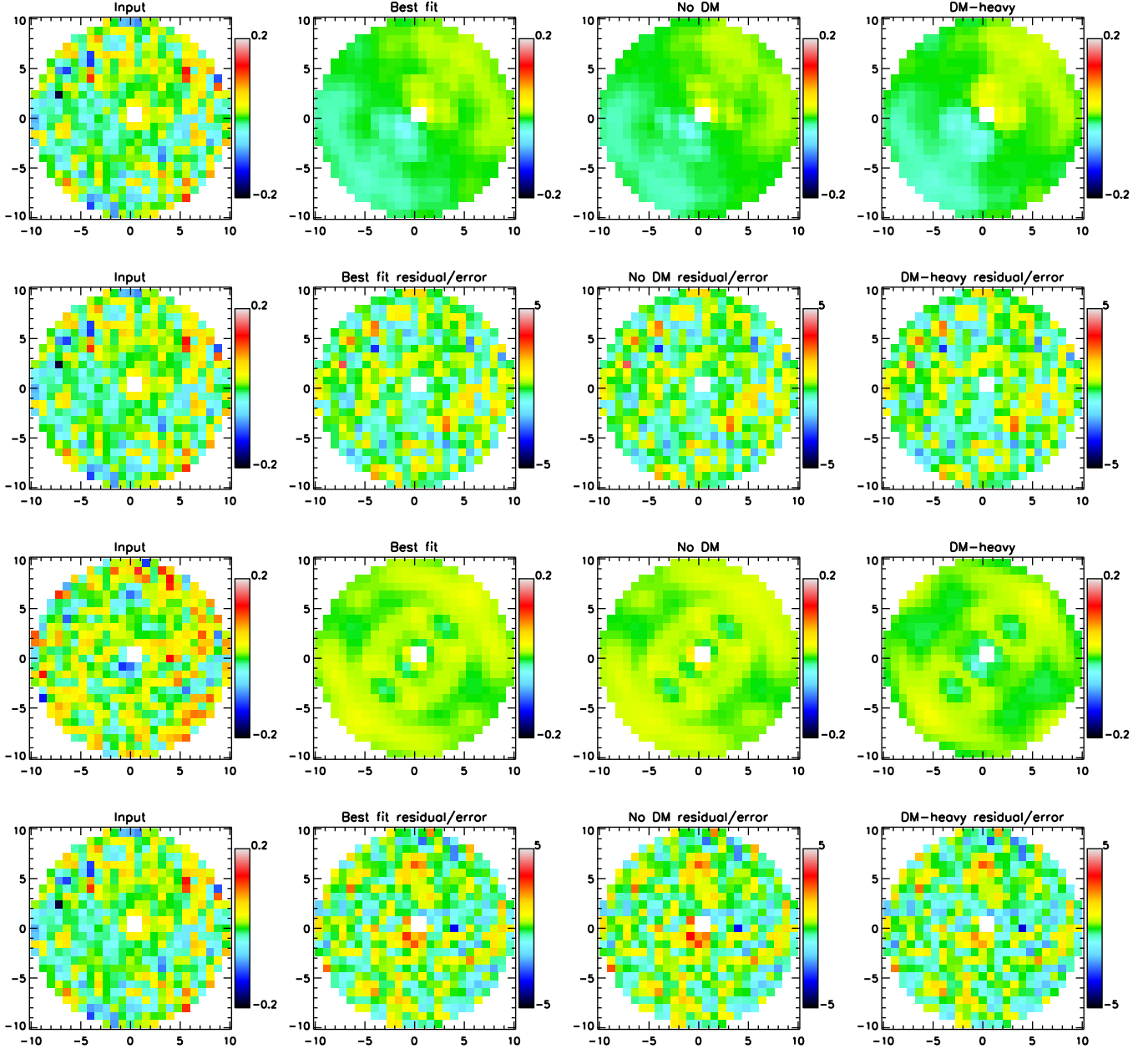


Figure 16. As in Figure 13, but for h_3 and h_4 from the SAURON data.

REFERENCES

- Adams, J. J., Blanc, G. A., Hill, G. J., et al. 2011, *The Astrophysical Journal Supplement Series*, 192, 5
- Arnold, J. A., Romanowsky, A. J., Brodie, J. P., et al. 2014, *ApJ*, 791, 80
- Bacon, R., Copin, Y., Monnet, G., et al. 2001, *MNRAS*, 326, 23
- Bai, L., Yee, H. K. C., Yan, R., et al. 2014, *ApJ*, 789, 134
- Barnabè, M., Czoske, O., Koopmans, L. V. E., Treu, T., & Bolton, A. S. 2011, *MNRAS*, 415, 2215
- Barro, G., Faber, S. M., Pérez-González, P. G., et al. 2013, *ApJ*, 765, 104
- Bender, R., Saglia, R. P., & Gerhard, O. E. 1994, *MNRAS*, 269, 785
- Blanc, G. A., Weinzirl, T., Song, M., et al. 2013, *AJ*, 145, 138
- Blanton, M. R., & Roweis, S. 2007, *AJ*, 133, 734
- Blumenthal, G. R., Faber, S. M., Primack, J. R., & Rees, M. J. 1984, *Nature*, 311, 517
- Bournaud, F., Jog, C. J., & Combes, F. 2007, *A&A*, 476, 1179
- Cappellari, M. 2002, *MNRAS*, 333, 400
- Cappellari, M. 2008, *MNRAS*, 390, 71
- Cappellari, M. 2013, *ApJ*, 778, L2
- Cappellari, M. 2016, *ARA&A*, 54, in press (arXiv:1602.04267)
- Cappellari, M., & Copin, Y. 2003, *MNRAS*, 342, 345
- Cappellari, M., & Emsellem, E. 2004, *PASP*, 116, 138

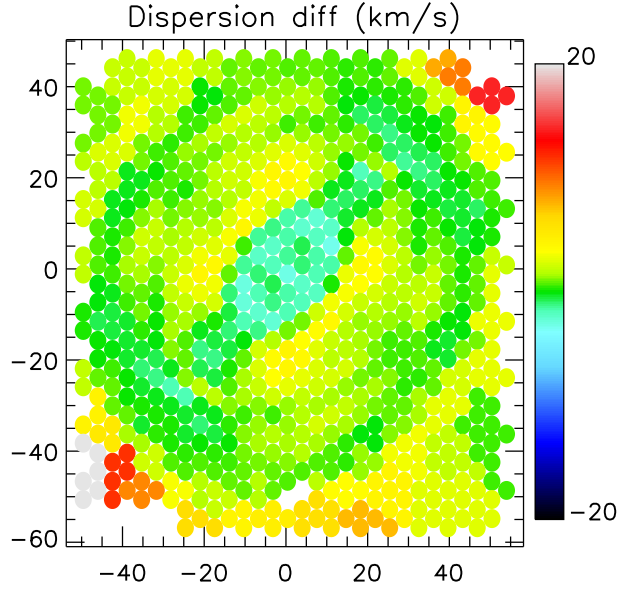


Figure 17. Difference in line of sight velocity dispersion between the selected DM-heavy model and the best-fit model, where a positive number indicates the former model being higher. The dispersion is somewhat higher over much of the FOV beyond $1R_e$, which is the main cause of the DM-heavy model's higher χ^2 .

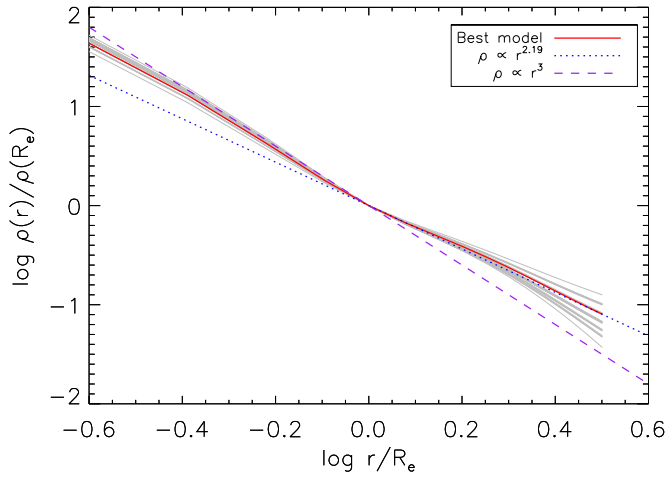


Figure 18. Total (dark plus baryonic) density profiles of all allowed Schwarzschild models, with lines for $\rho \propto r^{2.19}$ (Cappellari et al. 2015) and $\rho \propto r^3$ shown for comparison. We find the profiles to follow near-isothermal behaviour beyond the central effective radius, in good agreement with (Cappellari et al. 2015).

- Cappellari, M., Emsellem, E., Bacon, R., et al. 2007, MNRAS, 379, 418
 Cappellari, M., Emsellem, E., Krajnović, D., et al. 2011, MNRAS, 413, 813
 Cappellari, M., Scott, N., Alatalo, K., et al. 2013a, MNRAS, 432, 1709
 Cappellari, M., McDermid, R. M., Alatalo, K., et al. 2013b, MNRAS, 432, 1862
 Cappellari, M., Romanowsky, A. J., Brodie, J. P., et al. 2015, ApJ, 804, L21
 Cimatti, A., Nipoti, C., & Cassata, P. 2012, MNRAS, 422, L62

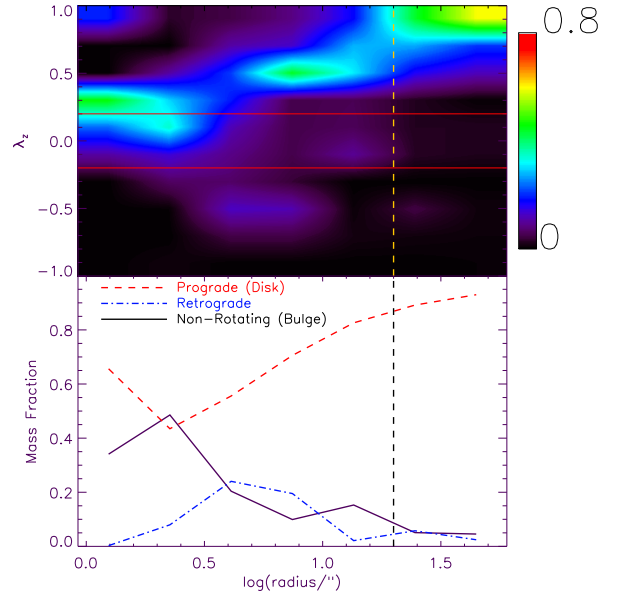


Figure 19. Mass distribution of orbits for the best-fitting orbit model, plotted as a function of average radius and spin. The distribution on the top panel is normalised per unit radius. The vertical dashed lines mark $1 R_e$. A bulge-disc separation is evident, with the disc coming to dominate in the outer observed regions.

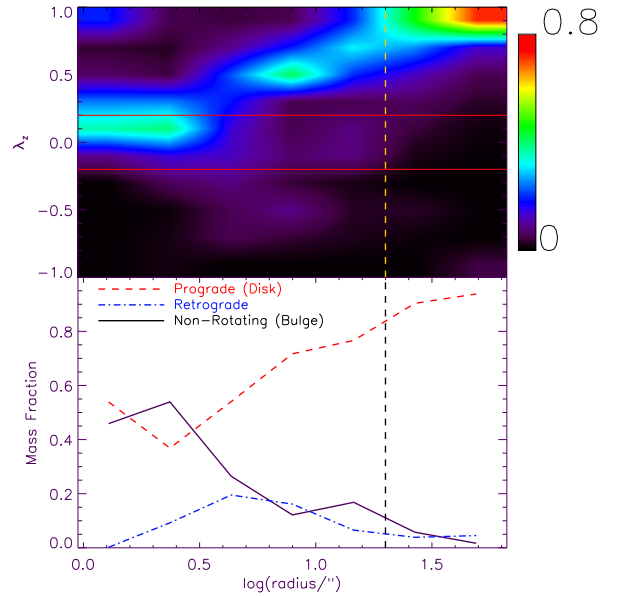


Figure 20. Same as Figure 19, but for the DM-free model.

- Coccatto, L., Arnaboldi, M., & Gerhard, O. 2013, MNRAS, 436, 1322
 de Zeeuw, P. T., Bureau, M., Emsellem, E., et al. 2002, MNRAS, 329, 513
 Douglas, N. G., Napolitano, N. R., Romanowsky, A. J., et al. 2007, ApJ, 664, 257
 Dressel, L. L., & Gallagher, J. S. 2001, in Astronomical Soci-

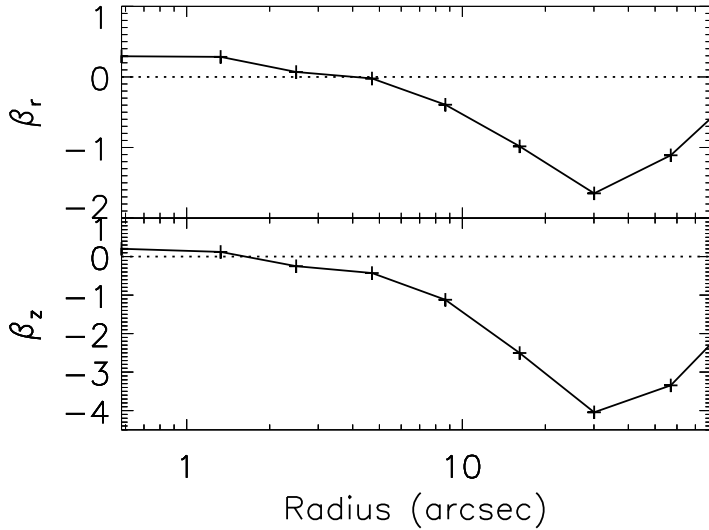


Figure 21. Orbital anisotropy parameters β_r (top) and β_z (bottom) for the best-fitting model, plotted as a function of radius along the galaxy major axis. The dotted lines represent isotropy. We find the orbital anisotropy to vary significantly as a function of position.

ety of the Pacific Conference Series, Vol. 249, The Central Kiloparsec of Starbursts and AGN: The La Palma Connection, ed. J. H. Knapen, J. E. Beckman, I. Shlosman, & T. J. Mahoney, 298

Emsellem, E., Monnet, G., & Bacon, R. 1994, *A&A*, 285, 723
 Emsellem, E., Cappellari, M., Krajnović, D., et al. 2007, *MNRAS*, 379, 401
 —. 2011, *MNRAS*, 414, 888
 Foster, C., Pastorello, N., Roediger, J., et al. 2016, *MNRAS*, 457, 147
 Gould, N. I. M., Orban, D., & Toint, P. L. 2003, *ACM Trans. Math. Softw.*, 29, 353
 Hill, G. J., MacQueen, P. J., Smith, M. P., et al. 2008, in *Astronomical Telescopes and Instrumentation: Synergies Between Ground and Space*, International Society for Optics and Photonics, 701470–701470
 Hoffman, L., Cox, T. J., Dutta, S., & Hernquist, L. 2010, *ApJ*, 723, 818
 Kelson, D. D. 2003, *Publications of the Astronomical Society of the Pacific*, 115, 688
 Khoperskov, S. A., Moiseev, A. V., Khoperskov, A. V., & Saburova, A. S. 2014, *MNRAS*, 441, 2650
 Krajnović, D., Cappellari, M., de Zeeuw, P. T., & Copin, Y. 2006, *MNRAS*, 366, 787
 Krajnović, D., McDermid, R. M., Cappellari, M., & Davies, R. L. 2009, *MNRAS*, 399, 1839
 Krajnović, D., Emsellem, E., Cappellari, M., et al. 2011, *MNRAS*, 414, 2923
 Krajnović, D., Alatalo, K., Blitz, L., et al. 2013, *MNRAS*, 432, 1768
 Kronawitter, A., Saglia, R. P., Gerhard, O., & Bender, R. 2000, *A&AS*, 144, 53
 Leauthaud, A., Tinker, J., Bundy, K., et al. 2012, *ApJ*, 744, 159
 Lin, L., Jian, H.-Y., Foucaud, S., et al. 2014, *ApJ*, 782, 33
 Magorrian, J., & Ballantyne, D. 2001, *MNRAS*, 322, 702
 McDermid, R. M., Alatalo, K., Blitz, L., et al. 2015, *MNRAS*, 448, 3484
 Naab, T., Johansson, P. H., & Ostriker, J. P. 2009, *ApJ*, 699, L178

Naab, T., Oser, L., Emsellem, E., et al. 2014, *MNRAS*, 444, 3357
 Navarro, J. F., Frenk, C. S., & White, S. D. M. 1996, *ApJ*, 462, 563
 Oser, L., Naab, T., Ostriker, J. P., & Johansson, P. H. 2012, *ApJ*, 744, 63
 Oser, L., Ostriker, J. P., Naab, T., Johansson, P. H., & Burkert, A. 2010, *ApJ*, 725, 2312
 Pota, V., Forbes, D. A., Romanowsky, A. J., et al. 2013, *MNRAS*, 428, 389
 Prugniel, P., & Soubiran, C. 2001, *A&A*, 369, 1048
 Querejeta, M., Eliche-Moral, M. C., Tapia, T., et al. 2015, *A&A*, 579, L2
 Raskutti, S., Greene, J. E., & Murphy, J. D. 2014, *ApJ*, 786, 23
 Remus, R.-S., Burkert, A., Dolag, K., et al. 2013, *ApJ*, 766, 71
 Röttgers, B., Naab, T., & Oser, L. 2014, *MNRAS*, 445, 1065
 Sánchez-Blázquez, P., Peletier, R. F., Jiménez-Vicente, J., et al. 2006, *MNRAS*, 371, 703
 Sánchez-Conde, M. A., & Prada, F. 2014, *MNRAS*, 442, 2271
 Schwarzschild, M. 1979, *ApJ*, 232, 236
 Scott, N., Cappellari, M., Davies, R. L., et al. 2013, *MNRAS*, 432, 1894
 Serra, P., Oosterloo, T., Morganti, R., et al. 2012, *MNRAS*, 422, 1835
 Trujillo, I., Förster Schreiber, N. M., Rudnick, G., et al. 2006, *ApJ*, 650, 18
 van de Ven, G., de Zeeuw, P. T., & van den Bosch, R. C. E. 2008, *MNRAS*, 385, 614
 van den Bosch, R. C. E., & de Zeeuw, P. T. 2010, *MNRAS*, 401, 1770
 van den Bosch, R. C. E., & van de Ven, G. 2009, *MNRAS*, 398, 1117
 van den Bosch, R. C. E., van de Ven, G., Verolme, E. K., Cappellari, M., & de Zeeuw, P. T. 2008, *MNRAS*, 385, 647
 van Dokkum, P. G. 2001, *PASP*, 113, 1420
 van Dokkum, P. G., Whitaker, K. E., Brammer, G., et al. 2010, *ApJ*, 709, 1018
 van Dokkum, P. G., Leja, J., Nelson, E. J., et al. 2013, *ApJ*, 771, L35
 van Dokkum, P. G., Nelson, E. J., Franx, M., et al. 2015, *ApJ*, 813, 23
 Walsh, J. L., van den Bosch, R. C. E., Barth, A. J., & Sarzi, M. 2012, *ApJ*, 753, 79
 Weijmans, A.-M., Cappellari, M., Bacon, R., et al. 2009, *MNRAS*, 398, 561
 Weijmans, A.-M., de Zeeuw, P. T., Emsellem, E., et al. 2014, *MNRAS*, 444, 3340
 Wu, X., Gerhard, O., Naab, T., et al. 2014, *MNRAS*, 438, 2701
 Yıldırım, A., van den Bosch, R. C. E., van de Ven, G., et al. 2015, *MNRAS*, 452, 1792
 —. 2016, *MNRAS*, 456, 538